Available online at www.sciencedirect.com
ScienceDirect
Trans. Nonferrous Met. Soc. China 32(2022) 79−90
Transactions of Nonferrous Metals Society of China
www.tnmsc.cn

Simulation on microstructure evolution of Al−Si alloy under effect of natural convection during solidification

Zhen-hong WANG[1,2], Li-tong ZHANG[1], Bin SU[2], Xiao-peng ZHANG[2]

1. Science and Technology on Thermostructural Composite Materials Laboratory, Northwestern Polytechnical University, Xi'an 710072, China;
2. Institute of Materials, China Academy of Engineering Physics, Jiangyou 621908, China

Received 7 December 2020; accepted 23 June 2021

Abstract: The solidification microstructure of Al−Si alloy was observed in the experiment, the second dendrite arm spacing (SDAS) was measured, and the effect of temperature on the microstructure was analyzed. Phase-field (PF) model incorporating natural convection caused by gravity was employed to simulate the microstructure evolution of Al−Si alloy under the experimental conditions. Good agreements between the experimental and simulation results verified the reliability of the simulation approach proposed in this study. Based on the proposed model, a series of simulation cases (2D and 3D) were performed to investigate the evolution of columnar and equiaxed dendritic structures. It was found that the solute content of the alloy had little impact on the microstructure evolution, while the solute expansion coefficient had obvious effect on the dendrite tip velocities. Significant improvement of computational efficiency was achieved via novel algorithms, making it possible to perform massive simulation for studying the evolution of solidification microstructures, which is hard to be directly observed in experiments via synchrotron radiation for Al−Si alloy.

Key words: Al−Si alloy; solidification microstructure; natural convection; phase-field simulation

1 Introduction

The aluminum−silicon (Al−Si) alloy is a kind of cheap and widely-used alloy, which plays an irreplaceable role in automobile industry because of its excellent properties, such as low density, high strength and heat durability as well as outstanding performance on mobility and mold filling in liquid phase. Besides, Al−Si alloy has ideal resistance of corrosion and good adaptability to extreme conditions, making it an important kind of material in military industry as well [1−4]. Thus, the research of Al−Si alloy's solidification features and the development of processing techniques are becoming vital national plans of the countries all over the world [5−9]. Currently, the research about Al−Si alloy has been mainly focused on experiments. GE [10] and LI [11] have studied the effect of heating conditions on the state of primary Si of the hypereutectic Al−20%Si alloy, and found that the prolonged heat preservation could obviously obtund the sharp corners of primary Si particles and coarsen the primary Si phases, which was unfavorable for ameliorating the Si particles. LIANG [12] has prepared the semi-solid Al−Si alloy based on the equilibrium heating technique, and analyzed the effect of flow field inside the semi-solid slurry on the microstructure evolution of Al−Si alloy, and proposed that the steady flow was helpful for obtaining the refined and evenly-distributed primary solid phase. ZHENG et al [13] have studied the impact of rheology parameters of die-casting craft on the microstructure and

Corresponding author: Xiao-peng ZHANG, Tel: +86-816-3626328, E-mail: saviorggg@163.com
DOI: 10.1016/S1003-6326(21)65779-5

mechanical properties of Al−30%Si alloy, and concluded that the vibration of "S"-shaped channel contributed greatly to the refinement of primary Si particles.

To date, most of the research about Al−Si alloy has mainly concerned the characterization of solidified microstructure, and the solidification process has rarely been reported. It is acknowledged that the microstructure is determined by the solidification process, thus elaborate investigation on the solidification process of Al−Si alloy should be performed in order to reveal the solidification features. Nevertheless, it is inconvenient to directly observe the microstructure evolution during solidification via synchrotron X-ray tomographic quantification, due to the large difference of the melting points of silicon (1410 °C) and aluminum (660 °C) [14].

Numerical simulation has been proved to be an effective solution to the problems mentioned above. In the field of metal solidification, phase-field (PF) method is a full-fledged and reliable approach which has kept developing in recent years, and the accuracy of the mathematical model and varieties of derived algorithms concerning PF method have been widely acknowledged [15−18]. DOBRAVEC et al [19] have proposed a novel numerical procedure to assess and reduce the discretization-induced anisotropy in the solution of the phase-field model for dendritic growth. In this study, the solidification process of Al−Si alloy was focused, and the microstructure evolution was demonstrated by simulation based on PF method. In most of the studies involving PF, the gravity was neglected in order to simplify the calculation. But in this study, the gravity was considered as a key factor which affected the microstructure evolution, since natural convection could be caused by mild density difference, which was inevitable because of the inhomogeneity of interdendritic solute distribution. The natural convection, which was coupled into the phase-field equations, was simulated by employing Lattice Boltzmann method (LBM). Besides, the algorithms of parallel computing and adaptive mesh refinement (AMR) were applied to guaranteeing the computational efficiency. The experimental and simulation results were compared to validate the coupling approach. A series of simulation cases (2D and 3D) were performed to reveal the microstructure evolution during the solidification of Al−Si alloy.

2 Experiments to obtain solidification microstructure

Experiments were performed to observe the solidification microstructure and compare with the simulation results, thus the experimental setup and procedures were not presented here in detail. The sample of Al−Si alloy was heated up by electron-magnetic conduction to 1400 °C, and cooled down to room temperature under different cooling conditions. A sample with sizes of d10 mm × 2 mm was obtained by wire-electrode cutting, and the microstructure of the sample was observed via SEM after the electrolytic-etching process. Figures 1(a−d) demonstrate the microstructures obtained at undercoolings of 20, 10, 5 and 1 °C, respectively. It could be seen that the cooling conditions had a significant effect on the microstructure evolution. Lower undercoolings resulted in denser dendritic structures, while the second dendrite arms became sparser and even disappeared as the undercooling increased, because the microstructure coarsening was closely related to the undercooling, and the microstructure was more prone to coarsen under a higher undercooling. The severest coarsening occurred in the microstructure shown in Fig. 1(a), where the dendritic structures scarcely appeared. In Fig. 1(b) only a few dendritic structures occupied the solidification zone, and in Figs. 1(c) and (d) the coarsening was dramatically alleviated, as can be seen in Fig. 1(d) that almost all primary trunks had secondary arms.

3 Mathematical model and numerical approach

The simulation was based on the following assumptions: (1) phase change and solute diffusion inside the solid were neglected; (2) there were no bubbles or inclusions existing in the melt which was considered as incompressible fluid; (3) the translational or rotational motion and the breaking of dendrites did not occur during solidification; (4) the release of latent heat of Al−Si alloy was not included in the simulation.

The governing equations of PF incorporating flow-field are given in Eqs. (1) and (2), which

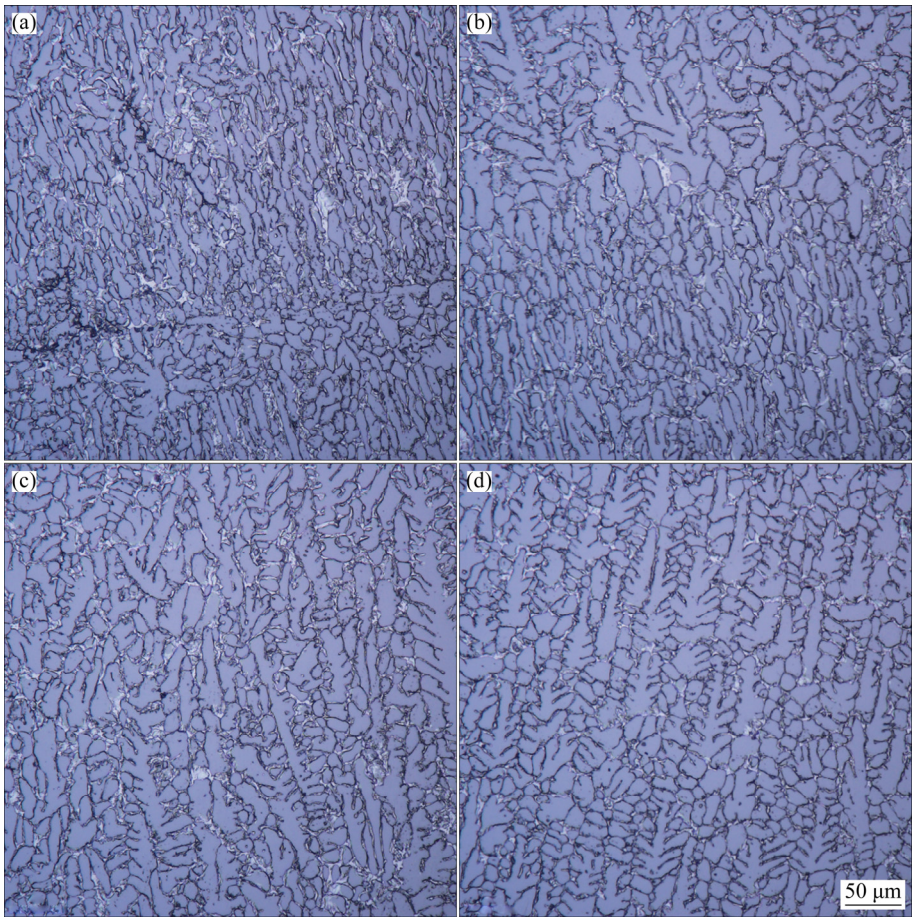

Fig. 1 Solidification microstructures of Al−Si alloy under different undercoolings: (a) 20 °C; (b) 10 °C; (c) 8 °C; (d) 1 °C

describe the relationship between PF variable ϕ and solute concentration U, undercooling θ, as well as the velocity vector $\boldsymbol{v}$. It can be seen from Eq. (2) that the flow-field contributes to the microstructure evolution by changing solute distribution.

$$\tau_\phi \frac{\partial \phi}{\partial t} = \nabla \cdot \left(W(\boldsymbol{n})^2 \nabla \phi \right) + \frac{\partial}{\partial x}\left(|\nabla \phi|^2 W(\boldsymbol{n}) \frac{\partial W(\boldsymbol{n})}{\partial \phi_x} \right) + \frac{\partial}{\partial y}\left(|\nabla \phi|^2 W(\boldsymbol{n}) \frac{\partial W(\boldsymbol{n})}{\partial \phi_y} \right) + \frac{\partial}{\partial z}\left(|\nabla \phi|^2 W(\boldsymbol{n}) \frac{\partial W(\boldsymbol{n})}{\partial \phi_z} \right) + \phi\left(1-\phi^2\right) - \lambda\left(1-\phi^2\right)^2 (\theta + U) \quad (1)$$

$$\left(\frac{1+k}{2} - \frac{1-k}{2}\phi \right) \frac{\partial U}{\partial t} = \nabla \cdot \left(D \frac{1-\phi}{2} \nabla U + \frac{W_0}{2\sqrt{2}} [1+(1-k)U] \frac{\partial \phi}{\partial t} \frac{\nabla \phi}{|\nabla \phi|} \right) + \frac{1}{2}[1+(1-k)U] \frac{\partial \phi}{\partial t} - \frac{1}{2}\boldsymbol{v}\{[1+k-(1-k)\phi]\nabla U - [1+(1-k)U]\nabla \phi\} \quad (2)$$

where τ_ϕ is the relaxation time of PF variable ϕ; $W(\boldsymbol{n})$ is the anisotropic width of the diffusion interface, and $\boldsymbol{n}$ is the unit normal vector; k and D are the partition coefficient and the solute diffusivity, respectively; $\lambda(=15L\Delta T_0/(16HT_M))$ is the scaling parameter with its reciprocal measuring the energy barrier height H, T_M and L are the melting point and latent heat of the alloy, respectively; $U(=\{(2c/c_\infty)/[1+k-(1-k)\phi]-1\}/(1-k))$ and $\theta(=(T-T_M-mc_\infty)/\Delta T_0)$ are the expressions of dimensionless solute distribution and temperature, respectively, c stands for the solute concentration while c_∞ is the initial value of c, and ΔT_0 $(=|m|c_\infty(1-k)/k)$ stands for the temperature range of equilibrium solidification and, m is the liquidus slop in the phase diagram; $\boldsymbol{v}(=f_l\boldsymbol{v}_{act})$ is the superficial velocity, $f_l(=(1-\phi)/2)$ is the volume fraction of liquid, and $\boldsymbol{v}_{act}$ is the actual velocity. For Al−20%Si alloy in this study, k=0.15 and D=3×10^{-9} m^2/s, the solidus and liquidus temperatures are 577 and

682 °C, respectively.

Two patterns of solidification patterns were considered in this study according to real processes. One was the isothermal solidification, in which the microstructure evolution was completely driven by compositional undercooling as a result of the solute diffusion, the microstructure was equiaxed and θ=−0.2; the other was the solidification under a temperature gradient of 1 K/cm in simulation, and the microstructure thus evolved to be columnar.

Our previous study (i.e. Refs. [20,21], which gave a more detailed explanation on key parameters for the simulation such as the relaxation time and the width of diffusive interface) mainly discussed the effect of forced flow (~0.1 m/s) on the microstructure evolution. But in this study, we highlighted the solidification under natural convection, which was rather mild (flow speed of 10^{-5}−10^{-4} m/s) compared to the forced flow.

Gravity was added as a body force to flow-field equations, i.e., Lattice Boltzmann equations, which are expressed in Eqs. (3) and (4), in order to input the driving force of natural convection, the body force G_i is given in Eq. (5):

$$f_i(\boldsymbol{r}+\boldsymbol{e}_i\Delta t,t+\Delta t)= f_i(\boldsymbol{r},t)-\frac{\Delta t}{\tau}\left[f_i(\boldsymbol{r},t)-f_i^{\mathrm{eq}}(\boldsymbol{r},t)\right]+\Delta t\cdot G_i(\boldsymbol{r},t) \tag{3}$$

$$f_i^{\mathrm{eq}}(\boldsymbol{r},t)=\rho w_i\left[1+\frac{3(\boldsymbol{e}_i\cdot\boldsymbol{u})}{c^2}+\frac{9(\boldsymbol{e}_i\cdot\boldsymbol{u})^2}{c^4}-\frac{3\boldsymbol{u}\cdot\boldsymbol{u}}{2c^2}\right] \tag{4}$$

$$G_i(\boldsymbol{r},t)=\rho w_i\left[3\frac{\boldsymbol{e}_i-\boldsymbol{u}}{c^2}+9\frac{(\boldsymbol{e}_i\cdot\boldsymbol{u})\boldsymbol{e}_i}{c^4}\right]\cdot(\boldsymbol{G}_{\mathrm{D}}+\boldsymbol{G}_{\mathrm{B}}) \tag{5}$$

where f_i is the particle density distribution at location $\boldsymbol{r}$ and time t; $\boldsymbol{r}$ is the location of the particle; $\boldsymbol{e}_i$ is the microscopic velocity of the fluid particles; t is the time; Δt is the time step; ρ is the density of the fluid; w_i is the lattice constant depending on the chosen lattice scheme; $\boldsymbol{u}$ is the velocity vector of the fluid; $\boldsymbol{G}_{\mathrm{D}}$ stands for the dissipative drag force vector to satisfy the non-slip boundary condition at the solid−liquid interface; $\boldsymbol{G}_{\mathrm{B}}$ is the buoyancy force due to the concentration difference in the liquid.

$$\boldsymbol{G}_{\mathrm{D}}(\boldsymbol{r},t)=-\frac{2\rho\upsilon h}{W_0}\left(\frac{1+\phi}{2}\right)^2\cdot\boldsymbol{u} \tag{6}$$

where υ is the kinematic viscosity; h is a constant equal to 2.757; W_0 is the interface thickness.

The buoyancy effect [22] as a result of the difference of solute distribution in liquid phase is expressed in Eq. (7):

$$G_{\mathrm{B}}(\boldsymbol{r},t)=-\rho\boldsymbol{g}\beta_{\mathrm{C}}(c-c_\infty)\frac{1}{2}(1-\phi) \tag{7}$$

where $\boldsymbol{g}$ and β_{C} are the vector of gravity acceleration and the solute expansion coefficient, respectively. The lattice structures of the schemes of D2Q9 and D3Q15 [23], which were employed in 2D and 3D simulation, respectively, are illustrated in Fig. 2. The vectors of lattice components $\boldsymbol{e}_i$ for D2Q9 and D3Q15 are listed in Tables 1 and 2, respectively. The simulation parameters are listed in Table 3. As pointed out in Ref. [20], the time step in the simulation is $\mathrm{d}t=r_{\mathrm{dt}}\Delta x_{\min}^2/(2d_{\mathrm{m}}D)$, where r_{dt}(=0.8) is the size of spacing step, $\Delta x_{\min}$ is the spatial step of the minimum grid, d_{m} is the dimension of the problem, and the minimum and maximum spacings are 0.8 and 12.8, respectively.

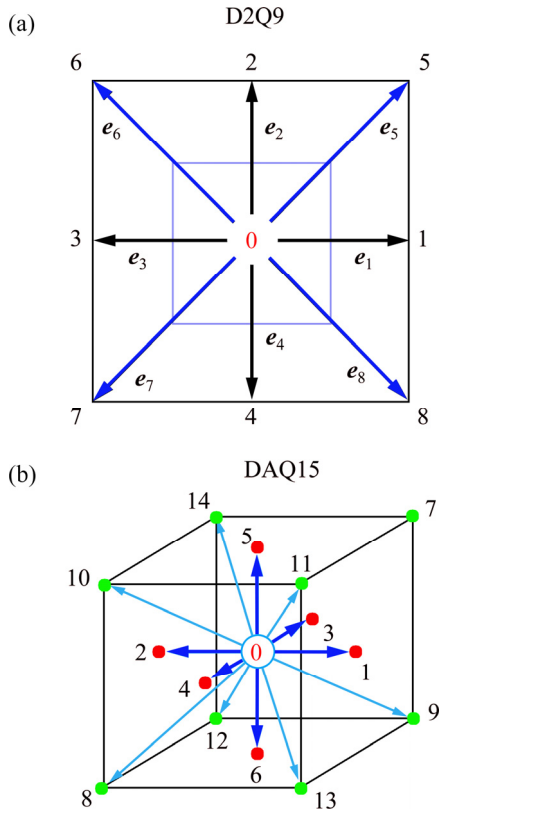

Fig. 2 Lattice structures of 2D (D2Q9) (a) and 3D (D3Q15) (b) simulation

Table 1 Vectors of lattice components for D2Q9 scheme

Direction	$\boldsymbol{e}_0$	$\boldsymbol{e}_1$	$\boldsymbol{e}_2$	$\boldsymbol{e}_3$	$\boldsymbol{e}_4$	$\boldsymbol{e}_5$	$\boldsymbol{e}_6$	$\boldsymbol{e}_7$	$\boldsymbol{e}_8$
x	0	1	0	−1	0	1	−1	−1	1
y	0	0	1	0	−1	1	1	−1	−1

Table 2 Vectors of lattice components for D3Q15 scheme

Direction	$\boldsymbol{e}_0$	$\boldsymbol{e}_1$	$\boldsymbol{e}_2$	$\boldsymbol{e}_3$	$\boldsymbol{e}_4$	$\boldsymbol{e}_5$	$\boldsymbol{e}_6$	$\boldsymbol{e}_7$	$\boldsymbol{e}_8$	$\boldsymbol{e}_9$	$\boldsymbol{e}_{10}$	$\boldsymbol{e}_{11}$	$\boldsymbol{e}_{12}$	$\boldsymbol{e}_{13}$	$\boldsymbol{e}_{14}$
x	0	1	−1	0	0	0	0	1	−1	1	−1	1	−1	1	−1
y	0	0	0	−1	1	0	0	−1	1	−1	1	1	−1	1	−1
z	0	0	0	0	0	1	−1	1	−1	−1	1	1	−1	−1	1

Table 3 Parameters for simulation cases

Case No.	Dimension	ε_1	ε_2	l_x	l_y	l_z	θ_y^-	θ_y^+	β_C	N
1	3D	0.15	0.00	1638.4	1638.4	1638.4	−0.12	−0.12	−1.4	1
2	2D	0.02	0.00	1638.4	1638.4	0	−0.12	−0.12	−10	1
3	2D	0.02	0.00	1638.4	1638.4	0	−0.12	−0.12	−5	1
4	2D	0.02	0.00	1638.4	1638.4	0	−0.12	−0.12	−1	1
5	2D	0.02	0.00	1638.4	1638.4	0	−0.12	−0.12	0	1
6	2D	0.02	0.00	1638.4	1638.4	0	−0.12	−0.12	1	1
7	2D	0.02	0.00	1638.4	1638.4	0	−0.12	−0.12	5	1
8	2D	0.02	0.00	1638.4	1638.4	0	−0.12	−0.12	10	1
9	2D	0.02	0.00	3276.8	3276.8	0	−0.13	−0.12	−1.4	10
10	2D	0.02	0.00	3276.8	3276.8	0	−0.13	−0.12	8.9	10
11	2D	0.02	0.00	3276.8	3276.8	0	−0.13	−0.12	−3.5	10
12	3D	0.15	0.00	1638.4	1638.4	1638.4	−0.14	−0.12	−1.4	10
13	3D	0.15	0.00	1638.4	1638.4	1638.4	−0.12	−0.12	−1.4	20
14	3D	0.15	0.00	1638.4	1638.4	1638.4	−0.14	−0.12	−1.4	10
15	3D	0.15	0.00	1638.4	1638.4	1638.4	−0.12	−0.12	−1.4	15

ε_1 and ε_2 are the magnitudes of the anisotropy strength favoring the crystalline orientations of [100] and [110], respectively; l_x, l_y and l_z are the lengths of the simulation zone along the coordinate axes of x, y and z, respectively; θ_y^- and θ_y^+ are the dimensionless temperatures at the cold and hot ends of the simulation zone, respectively; N stands for the number of grains in the simulation

4 Results and discussion

4.1 Comparison of experimental and simulation results

Figure 3(a) shows that the columnar dendritic structures dominated the solidification zone due to the temperature gradient. A large number of columnar dendrites appeared, most of the primary arms crossed with each other, and some of the primary arms had collapsed or been impeded from further evolution. The complexity of microstructure evolution made it hard to input simulation parameters which perfectly agreed with the experimental conditions. Nevertheless, the comparison of experimental and simulation results was still feasible based on the fact that the second dendrite arm spacing (SDAS) precisely revealed the solidification conditions. Provided that the kinetic and dynamic solidification conditions remained the same, SDAS remained constant whether the evolution space was sufficient or not. Consequently, the experimental and simulation results of SDAS were chosen for comparison in order to validate the numerical modeling. Figures 3(a) and (b) demonstrated that the average SDAS in the experiment agreed well with that in the simulation (with a deviation less than 3%), indicating that an ideal performance of numerical modeling was achieved in this study for the prediction of microstructure evolution of Al−Si alloy during the solidification.

4.2 Discussion

The boundary conditions for the simulation of microstructure evolution under natural convection are illustrated in Fig. 4. All the walls in 2D and 3D cases were non-slip, and the gravity was opposite to

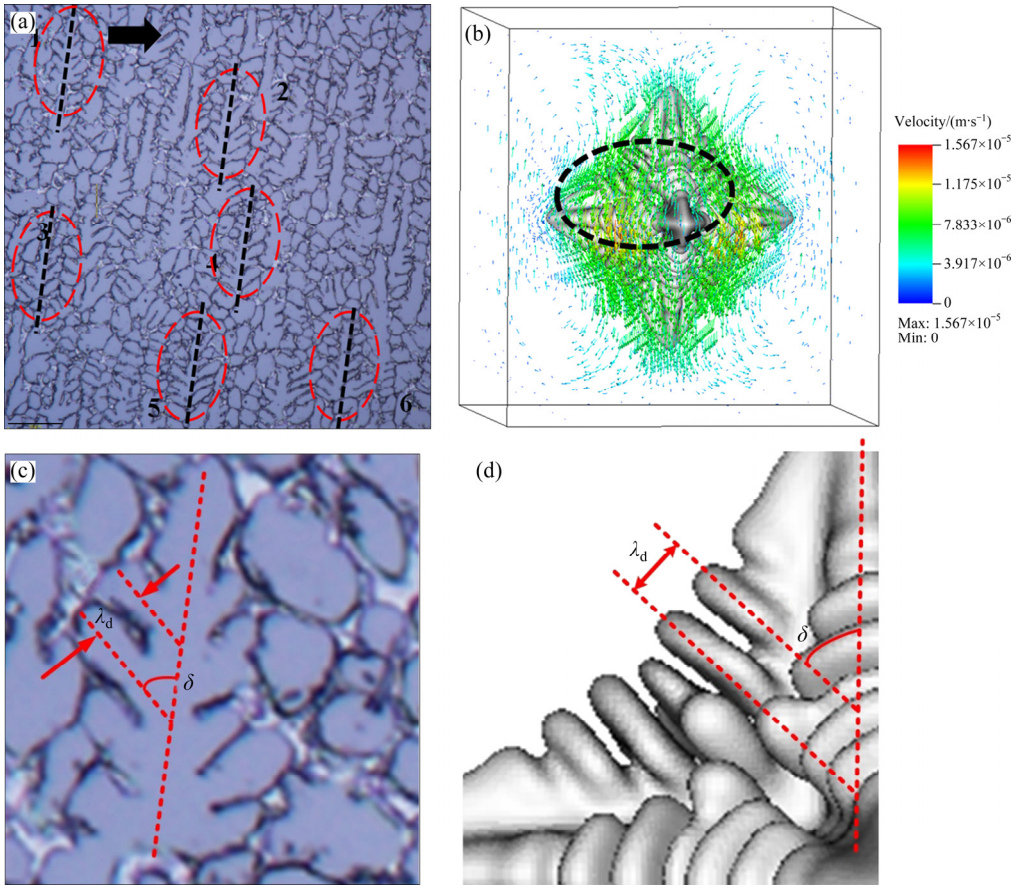

Fig. 3 Comparison of microstructures obtained by experiment and simulation (corresponding to Case 1): (a) Experimental results; (b) Simulation results; (c) Enlarged map of zoomed area in (a); (d) Enlarged map of zoomed area in (b)

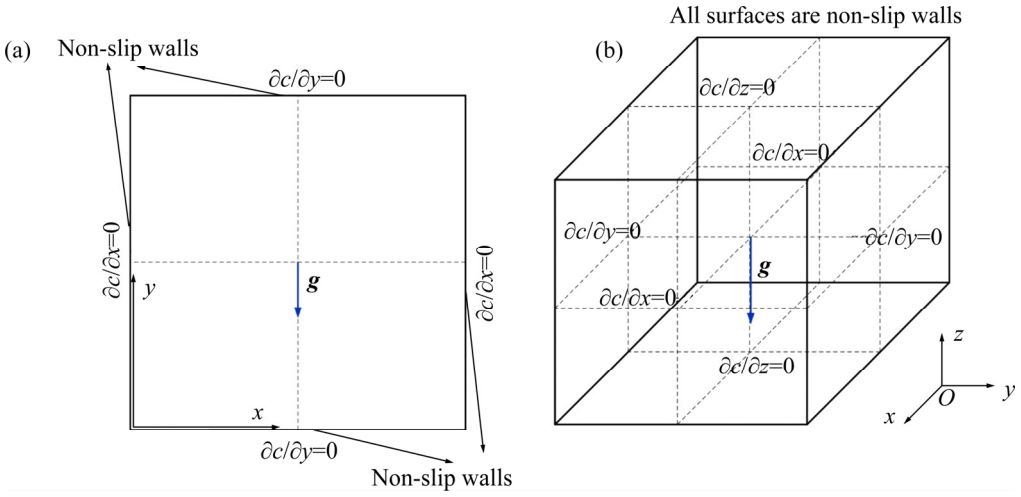

Fig. 4 Boundary conditions for simulation of microstructure evolution: (a) 2D case; (b) 3D cases

the growth direction, i.e. the direction of y axis for 2D case and the direction of z axis for 3D case. For all non-slip boundaries, $\partial c/\partial \xi=0$, where ξ was the axis normal to the boundary. Natural convection was supposed to be driven by the body force resulted from the difference of solute concentration. During solidification the equiaxed dendrite grains nucleated randomly in the whole zone, while the columnar ones initiated from the bottom and evolved upward. The bounce back scheme [20] was applied to treating the boundaries of dendritic blocks inside the solidification zone.

TAKAKI et al [22] pointed out that the natural convection in varieties of alloys during the

solidification was significantly different due to the difference of solute expansion coefficient β_C. In this study, β_C was adjusted for revealing its effect on the feature of natural convection, as well as on the solute distribution and dendrite morphology. When $\beta_C=0$, the solute could not burst into the liquid rapidly, and there was no solute migration during the solidification other than the diffusion on the solid−liquid interface. But virtually for all alloys, $\beta_C\neq0$, when $\beta_C>0$, if $c>c_0$, then $\boldsymbol{G}_B(\boldsymbol{r},t)<0$, i.e., the vector of body force was opposite to the gravity, resulting in the buoyancy effect which drove the solute upward; when $\beta_C<0$, if $c>c_0$, then $\boldsymbol{G}_B(\boldsymbol{r},t)>0$, i.e., the solute descended into the dendritic gaps as the direction of body force was the same as that of gravity. β_C revealed the spreading speed of solute into the liquid, and larger $|\beta_C|$ meant faster solute motion and more intensive natural convection. As demonstrated in Fig. 5, the dendrite morphology and solute distribution varied significantly in the

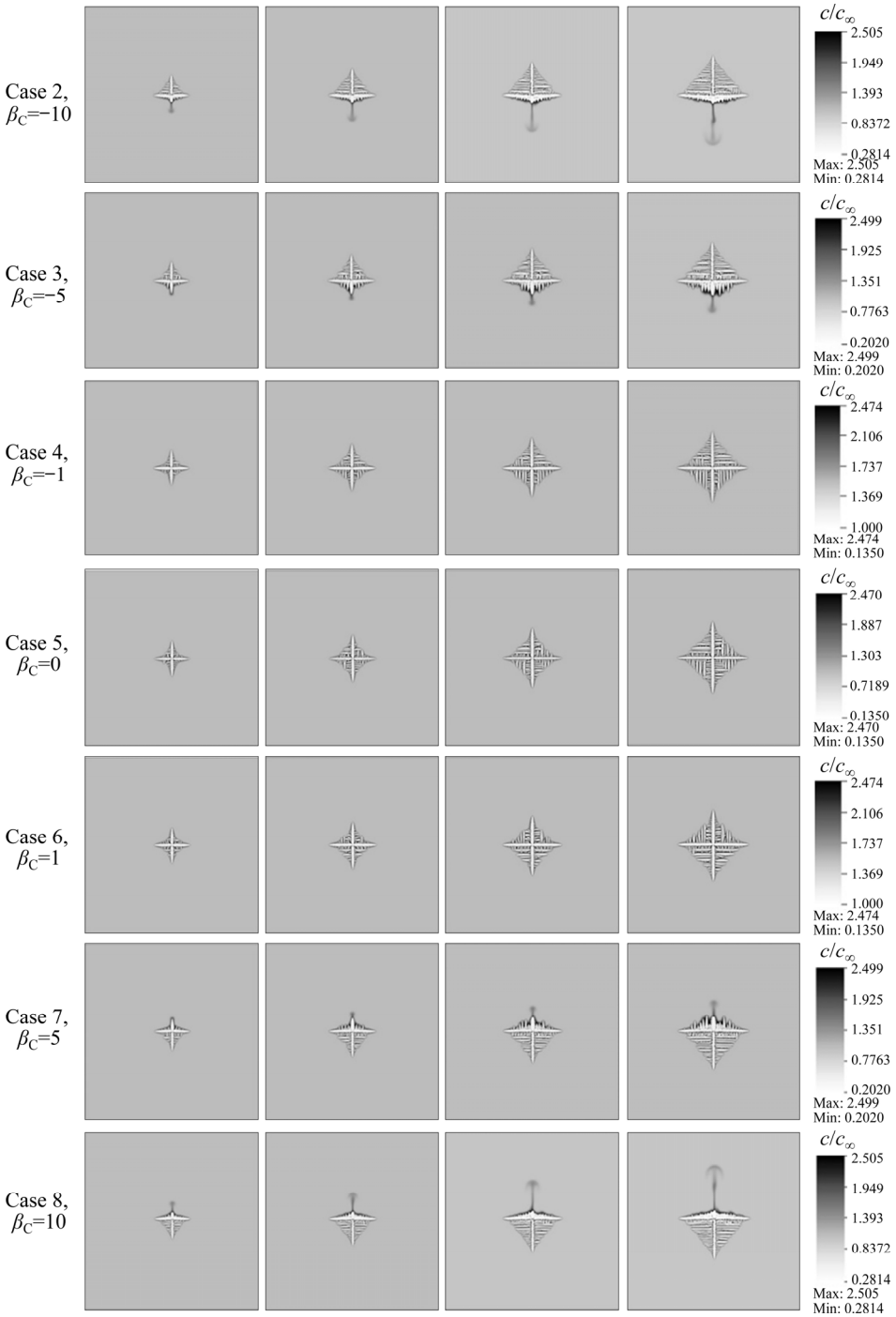

Fig. 5 Effects of β_C on dendrite morphology and solute motion

cases with different β_C values (0, 1, 5, 10). As mentioned above, there was buoyancy when β_C=0, and even when $|\beta_C|$ increased to 1, the solute distribution scarcely changed as the natural convection was too weak to promote the solute motion. Accordingly little change could be discerned in dendritic structure. In one half zone, the growth of secondary dendrite arms, which was suppressed in the normal direction, proceeded only along the horizontal direction; in the other half zone, the dendrite evolution was promoted along the normal direction, while the horizontal growth was restrained. It could be concluded that the suppression or promotion of dendrite growth was closely related to the speed of solute precipitation. In the case of $|\beta_C|$=5, the moving ability of solute was so obviously improved that heavy accumulation appeared peripherally near the solid−liquid interface, leading to a sharp decrease of local undercooling and a remelting of microstructures, and the dendrite evolution became much slower than that in the case of $|\beta_C|$<5. As $|\beta_C|$ further increased to 10, more intensive solute motion into the melt as well as severer solute accumulation outwards the solid−liquid interface could be observed, and the dendrite evolution almost ceased due to the lack of essential undercooling.

The simulation results of the microstructure evolution of Al−Si alloy under the effect of natural convection are shown in Fig. 6(a), where 10 grains initiated at the bottom and grew upward, and different colors were displayed in order to distinguish different grains. The solute Si of the alloy with β_C=−1.4 precipitated into the interdendritic gaps during solidification as the density of Si was slightly higher than that of the melt, but the density difference was almost negligible, i.e., β_C was so mild that the motion propensity of Si in the alloy was rather weak. The simulation of the microstructure evolution of another two kinds of alloys (Ga−25%In and Al−4%Cu) and the comparison of the simulation results between them were performed in order to highlight the effect of β_C on solidification microstructures. The β_C values of Ga−25%In and Al−4%Cu alloy are 8.9 and −3.5, respectively, both much higher than that of Al−Si alloy, implying much more intensive solute motion in the two kinds of alloys. As can be seen in Figs. 6(b) and (c), for Ga−25%In alloy, of which the solute was much lighter than the melt, the solute In rose upward into the liquid during solidification due to a negative β_C; while for Al−4%Cu alloy, which had a heavier solute than the melt, the solute Cu precipitated into the gaps inside the dendritic networks as a result of a positive β_C.

Figure 7(a) illustrates the initial state of 10 grains planted at the bottom of solidification zone. For the alloys of Al−Si, Al−Cu and Ga−In, each grain labelled with the same number previously had

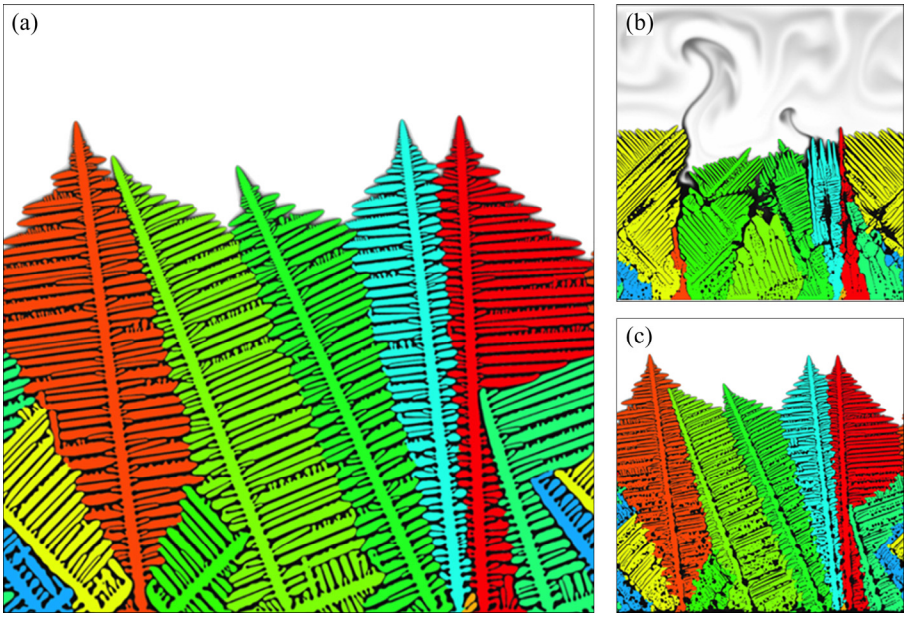

Fig. 6 Simulation results of microstructure evolution for alloys of Al−Si (Case 9, β_C=−1.4) (a), Ga−25%In (Case 10, β_C=8.9) (b) and Al−4%Cu (Case 11, β_C=−3.5) (c)

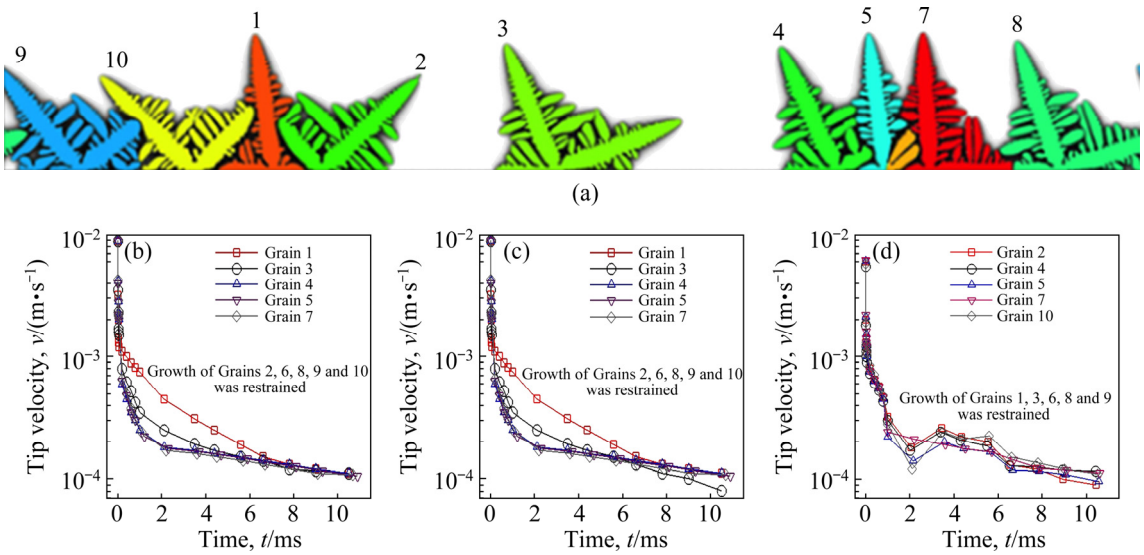

Fig. 7 Location and numbers of grains at initial stage (a) and tip velocities of grains of Al−Si (b), Al−Cu (c) and Ga−In (d) alloys

the same growth direction. It is apparent in Fig. 7(b) that the variation trends of tip velocity for the grains of Al−Si alloy were very close to each other, the tip velocity was the highest (nearly 10^{-2} m/s) at the beginning, and decreased quickly in a short span. As the solidification proceeded, the tip velocities tended to be more and more stabilized, and eventually reached nearly 10^{-4} m/s. The evolution of Grains 2, 6, 8, 9 and 10 was impeded during solidification by other dendrites, while Grains 1, 3, 4, 5 and 7 always kept growing, the trends of tip velocity of the grains whose evolution was not interrupted were similar. Figure 7(c) shows that the trends of tip velocity for Al−Cu and Al−Si alloys almost coincide with each other, except in the final solidification stage. However, significant difference can be seen in the trends of tip velocity between the alloys of Al−Si (Fig. 7(b)) and Ga−In (Fig. 7(d)), from the very beginning to the end. For Ga−In alloy, all the tip velocities were under 10^{-2} m/s, and all grains except Grain 7 experienced severe tip velocity fluctuation throughout the solidification, besides, the numbers of grains which kept evolving are 2, 4, 5, 7 and 10, quite different from the situation during the solidification of Al−Si alloy. It was summarized that β_C played a key role in determining tip velocities, which became more and more divergent with the increase of $|\beta_C|$.

The simulation results corresponding to Cases 12−15 are presented respectively in Figs. 8(a−d), from which, we can see that the morphology of equiaxed dendritic structures was evidently different from that of the columnar ones even for the same alloy. We set a temperature gradient for triggering the growth of columnar dendrites, i.e., $\theta_y^+ - \theta_y^- \neq 0$; while the evolution of equiaxed dendrites did not depend on temperature gradient, it was driven by the compositional undercooling caused by solute diffusion, $\theta_y^+ - \theta_y^-$ was thus set to be zero. The solute content was 10% for the cases in Figs. 8(a, b) and that was 15% for those in Figs. 8(c, d). From the simulation results it could be seen that the solute content had almost no effect on SDAS, i.e., no factors other than the temperature undercooling affected the SDAS, which coincided with the conclusion proposed by MADISON et al [24]. Besides, Fig. 8 shows that the solid fraction was closely related to natural convection, in Figs. 8(c, d) the flow field mainly distributed in the peripheral area near the dendrites, while in the melt far away from the solid, the convection was almost negligible. The natural convection gradually occupied the whole zone with increase of the solid fraction, as the flow field expanded with the promotion of solidification front. Natural convection (flow velocity generally within 10^{-4} m/s) in the solidification of Al−Si alloy, which was obviously different from the forced flow (above 10^{-2} m/s) described in our previous work [20,21], had little effect on the dendrite morphology. As shown in Fig. 3(b), the length of each primary arm of equiaxed dendrites was almost the same.

Figure 9 reveals the relationship between the computing time and the level of AMR (N_{amr}) as well as the number of processor units (N_p). For the cases with uniform meshes, i.e., N_{amr}=1, the computing overheads were rather considerable (over 1×10^5 s) even in 2D case; the computing efficiency was determined almost only by the number of processor units. The time cost decreased to 8704, 4015, 2312 and 1306 s as N_p increased to 24, 48, 96 and 192, respectively and the improvement of computing efficiency ceased after N_p exceeded 192, and it still cost 1287 s for simulation even when N_p was increased to 384. When N_{mar}=5, N_p similarly played an important role in guaranteeing computing efficiency, but the computing time, which decreased with the increase of N_p, reached a limitation when $N_p\geq96$. N_{amr} also had vital importance for shortening the computing time, for 2D case, the time cost was reduced nearly 50% with one more mesh level added. In this study, the elapsed time for simulation was shortened to 710 s by employing 24 processor units along with 5 mesh levels (N_p=24 and N_{amr}=5),

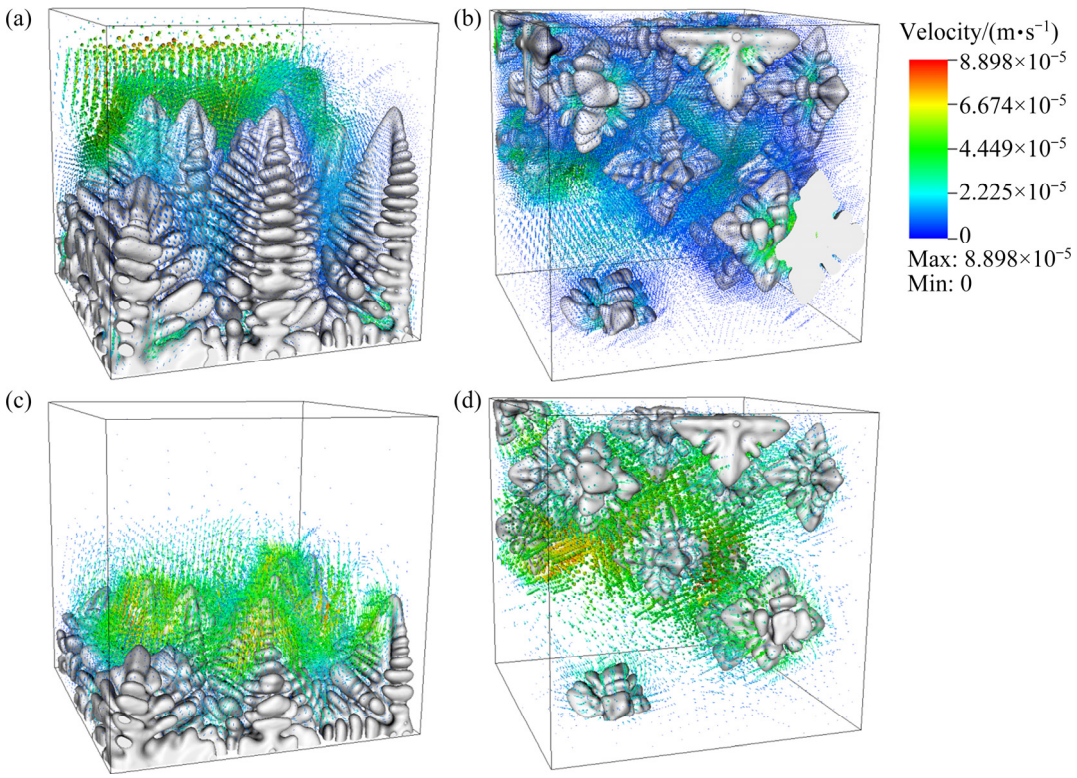

Fig. 8 Microstructure and distribution of flow field during solidification of Al−Si alloy under natural convection: (a, c) Columnar dendrites; (b, d) Equiaxed dendrites

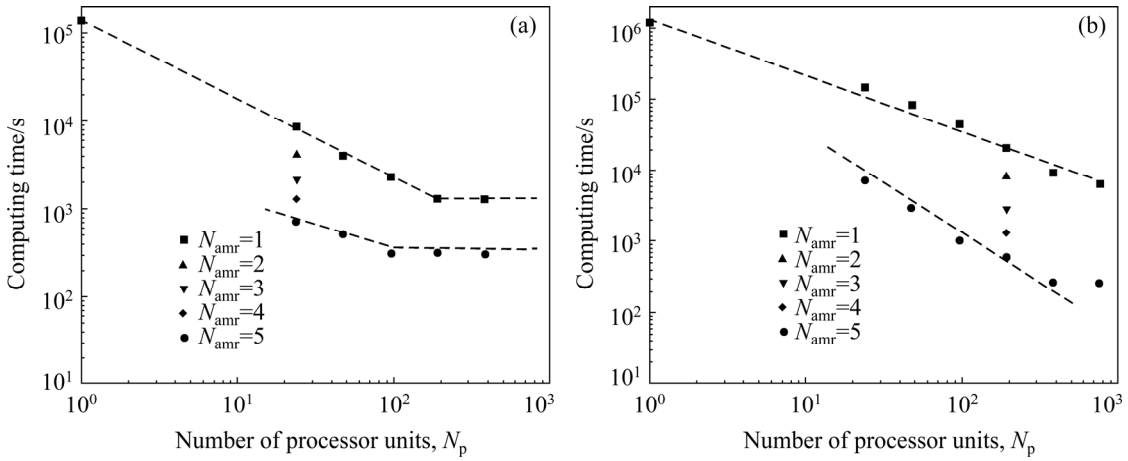

Fig. 9 Relationship among computing time, number of processor units N_p and level of AMR N_{amr}: (a) 2D case; (b) 3D case

while it cost 8704 s without mesh optimization (N_p=24 and N_{amr}=1), indicating that the computing efficiency was improved by nearly 12 times via AMR.

In 3D simulation with single processor unit at N_{amr}=1, tremendous computing time would be required, making it unsuitable for application; but the computation was sharply accelerated with the increase of N_p, similar trends could be found in the 2D cases. The relationship between computing time t_{simu} and N_p was expressed as follows:

$$\lg t_{simu}=k_c \lg N_p+\lg t_{simu}^{N_p=1} \quad (8)$$

where k_c was the slope, a constant determined by N_{amr}. For the simulation of 3D case with N_p=768, the time cost was t_{simu}=260 s, the acceleration of computation approached its limitation, as the discrepancy between the computing time of the two cases with 384 and 768 processor units was not obvious, when N_p=384, the required computing time slightly increased to t_{simu}=270 s. It can be seen that, the computing efficiency was greatly boosted due to the employment of AMR. For instance, when N_p=192, the efficiency of simulation was improved by 35 times via AMR with 5 mesh levels.

5 Conclusions

(1) The microstructure of Al−Si alloys in the directional solidification was observed via experiments, and the effect of thermal conditions on the microstructure morphology was analyzed. It was found that lower undercooling resulted in more prosperous evolution of dendritic structures, while higher undercooling promoted the coarsening of microstructures more obviously.

(2) LBM equations were coupled into the PF models in order to describe the natural convection during solidification. Based on that, the 3D simulation for the microstructure evolution of Al−Si alloy with different solute contents under natural convection was performed. The effect of solute expansion coefficient β_C on the microstructure evolution was figured out, revealing that Al−Si alloy was not vulnerable to common defects like freckles and channels as its β_C was not large.

(3) Simulation results of microstructure evolution for the alloy of Al−Si, Ga−In and Al−Cu were compared. It was found that the variation trends of the dendrite tip velocities were very similar between the alloys of Al−Si and Al−Cu as the parameter β_C was close with each other, and the tip velocity gradually decreased with the proceeding of solidification. However, for the alloy of Ga−In, intensive fluctuation of tip velocities occurred during solidification due to a large β_C. The computing efficiency was drastically improved (almost over 30 times) via the application of parallel computing as well as the algorithm of AMR especially for 3D case.

Acknowledgments

The authors are grateful for the financial supports from the National Key R&D Program of China (No. 2016YFB0701201) and the Fostering Project in Innovation Funds of China Academy of Engineering Physics (No. PY2019078). The authors acknowledge the Tianhe-2 in Guangzhou, China, for access to supercomputing facilities. The authors would like to thank AMReX for facilitating the application of AMR, and VisIt, on which the visualization of simulation results was performed. Dr. Xiao-peng ZHANG gratefully acknowledges the financial support from China Scholarship Council. Dr. Xiao-peng ZHANG would also like to thank Prof. Ming-fang ZHU and Prof. Dong-ke SUN in Southeast University, China, for fruitful discussion on employing the lattice Boltzmann method in phase-field modeling.

References

[1] GRUGEL R, KURZ W. Growth of interdendritic eutectic in directionally solidified Al−Si alloys [J]. Metallurgical and Materials Transactions A, 1987, 18: 1137−1142.

[2] LU S Z, HELLAWELL A. The mechanism of silicon modification in aluminum−silicon alloys: Impurity induced twinning [J]. Metallurgical and Materials Transactions A, 1987, 18: 1721−1733.

[3] LIANG D, BAYRAKTAR Y, JONES H. Formation and segregation of primary silicon in Bridgman solidified Al−18.3wt.%Si alloy [J]. Acta Metallurgica et Materialia, 1995, 43: 579−585.

[4] JIN Dao-cheng. Application of A356 alloy in the automobile industry [J]. Metal World, 2000, 3: 4−5. (in Chinese)

[5] HOSCH T, ENGLAND L G, NAPOLITANO R E. Analysis of the high growth-rate transition in Al−Si eutectic solidification [J]. Journal of Materials Science, 2009, 44: 4892−4899.

[6] ZABLER S, ERSHOV A, RACK A, GARCIA-MORENO F, BAUMBACH T, BANHART J. Particle and liquid motion in semi-solid aluminium alloys: A quantitative in situ

microradioscopy study [J]. Acta Materialia, 2013, 61: 1244−1253.
[7] LU Shu-zu, HELLAWELL A. Modification and refinement of cast Al−Si alloys [M]. Berlin: Springer International Publishing, 2016.
[8] ZAGULIAEV D, KONOVALOV S, IVANOV Y, GROMOV V. Effect of electron-plasma alloying on structure and mechanical properties of Al−Si alloy [J]. Applied Surface Science, 2019, 498: 143767.
[9] HUANG Xiu-song, DONG Xi-xi, LIU Le-hua, LI Pei-jie. Liquid structure of Al−Si alloy: A molecular dynamics simulation [J]. Journal of Non-Crystalline Solids, 2019, 503: 182−185.
[10] GE Liang-qi. Research on the control technique for the form of primary silicon in Al−20%Si alloy [D]. Nanjing: Nanjing University of Science and Technology, 2007. (in Chinese)
[11] LI Qing-lin. Research on the evolution of silicon phase and the performance of hypereutectic Al−20%Si alloy [D]. Lanzhou: Lanzhou University of Technology, 2014. (in Chinese)
[12] LIANG Xiao-kang. Study on the preparation technique and application of semisolid slurry of Al−Si alloy [D]. Beijing: General Research Institute for Nonferrous Metals, 2017. (in Chinese)
[13] ZHENG Zhi-kai, JI Yong-jian, MAO Wei-min, YUE Rui, LIU Zhi-yong. Influence of rheo-diecasting processing parameters on microstructure and mechanical properties of hypereutectic Al−30%Si alloy [J]. Transactions of Nonferrous Metals Society of China, 2017, 27: 1264−1272.
[14] CHOUHARY C, SAHOO K L, MANDAL D. Microstructure and mechanical properties of Al−Si alloys processed by strain induced melt activation [J]. Materials Today: Proceedings, 2018, 5: 27107−27111.
[15] OHNO M, TAKAKI T, SHIBUTA Y. Numerical testing of quantitative phase-field models with different polynomials for isothermal solidification in binary alloys [J]. Journal of Computational Physics, 2017, 335: 621−636.
[16] GUO Z P, MI J, XIONG S, GRANT P S. Phase field simulation of binary alloy dendrite growth under thermal- and forced-flow fields: An implementation of the parallel multigrid approach [J]. Metallurgical and Materials Transactions B, 2013, 44: 924−937.
[17] SAKANE S, TAKAKI T, ROJAS R, OHNO M, SHIBUTA Y, SHIMOKAWABE T, AOKI T. Multi-GPUs parallel computation of dendrite growth in forced convection using the phase-field-lattice Boltzmann model [J]. Journal of Crystal Growth, 2017, 474: 154−159.
[18] CORBELLA C, ECHEBARRIA B, RAMIREZ-PISCINA L, PASCUAL E, ANDUJAR J L, BERTRAN E. Growth kinetics of nanometric dendrites in metal–carbon thin films [J]. Acta Materialia, 2009, 57: 4948−4956.
[19] DOBRAVEC T, MAVRIC B, SARLER B. Reduction of discretisation-induced anisotropy in the phase-field modeling of dendritic growth by meshless approach [J]. Computational Materials Science, 2020, 172: 109166.
[20] ZHANG X, KANG J, GUO Z, XIONG S, HAN Q. Development of a para-AMR algorithm for simulating dendrite growth under convection using a phase-field-lattice Boltzmann method [J]. Computer Physics Communications, 2018, 223: 18−27.
[21] ZHANG X, KANG J, GUO Z, HAN Q. Effect of the forced flow on the permeability of dendritic networks: A study using phase-field-lattice Boltzmann method [J]. International Journal of Heat and Mass Transfer, 2019, 131: 196−205.
[22] TAKAKI T, ROJAS R, SAKANE S, OHNO M, SHIBUTA Y, SHIMOKAWABE T, AOKI T. Phase-field-lattice Boltzmann studies for dendritic growth with natural convection [J]. Journal of Crystal Growth, 2017, 15: 146−153.
[23] SUKOP M C, THORNE D T. Lattice Boltzmann modeling: An introduction for geoscientists and engineers [M]. New York: Springer, 2006.
[24] MADISON J, SPOWART J, ROWENHORST D, AAGESEN L K, THORNTON K, POLLOCK T M. Modeling fluid flow in three-dimensional single crystal dendritic structures [J]. Acta Materialia, 2010, 92: 8−17.

自然对流作用下 Al−Si 合金凝固过程的组织演变模拟

王震宏[1,2]，张立同[1]，苏 斌[2]，张小鹏[2]

1. 西北工业大学 超高温结构复合材料重点实验室，西安 710072；
2. 中国工程物理研究院 材料研究所，江油 621908

摘 要：通过实验观察 Al−Si 合金的凝固组织，测量枝晶组织的二次枝晶臂间距，并分析温度对凝固组织的影响。在相场模型中引入重力引起的自然对流以预测实验条件下 Al−Si 合金凝固组织的演变。模拟结果与实验结果吻合良好，验证了本文中提出的模拟方法的可靠性。基于本文的耦合模型，开展一系列不同溶质含量合金柱状晶和等轴晶组织生长的二维和三维模拟，发现合金中溶质含量对凝固组织的演变几乎没有影响，而溶质膨胀系数对枝晶尖端移动速度有显著影响。本文中采用的算法极大地加快计算效率，因此，大规模的数值模拟使难以直接通过同步辐射实验观察的 Al−Si 合金凝固组织演变过程的研究成为可能。

关键词：铝硅合金；凝固组织；自然对流；相场模拟

(Edited by Wei-ping CHEN)